

Efficiently Guided Active Contours for Image Segmentation

Lutful Mabood¹, Tahir Ullah², Haider Ali³, Noor Badshah⁴

^{1,2,3} Department of Mathematics, University of Peshawar, Pakistan.

⁴ Department of Basic Sciences, University of Engineering and Technology, Peshawar, Pakistan.

^{1,2,3,4} Email: lathizm@gmail.com, tahir khan264@gmail.com, haider_uop99@yahoo.com, noor2knoor@gmail.com

Received: 21 May, 2019 / Accepted: 22 July, 2021 / Published online: 9 July, 2022

Abstract. Segmenting natural and outdoor images are challenging for most of the latest variational segmentation models. For this purpose we employ derived image data (DID) and propose a robust variational model. The DID rely on three images by utilizing image local and global statistics as well as filter image which is obtained through our design high pass filtering techniques. Then these derived image data are incorporated into our proposed energy functional which can robustly segment images having inhomogeneity, mix backgrounds and multi-regions. Furthermore, the results of DID are compared with other well known methods with finding Jaccard similarity index to proof the efficient and qualitative performance of proposed model over the traditional methods. Finally, the proposed DID based model is tested on real world 3D images to ensure that it also preserve its performance in vector valued images as well.

AMS (MOS) Subject Classification Codes: 35S29; 40S70; 25U09

Key Words: Calculus of Variation, Functional Minimization, Level Sets and Partial Differential Equations.

1. INTRODUCTION

One of the important task in machine vision is image segmentation. The main theme of image segmentation is to distinguish objects from their background. For image segmentation a famous approach which caught attention of researchers very rapidly is variational methods. Variational approach is often implemented via active contour approach [3, 9, 13, 19, 21]. In active contour mechanism for the segmentation of a given image, either image derivative information [6, 7] is employed or image statistics [4, 18, 19] is used to derive the contour to identify the edges. The former one is edge-based approach while the later one is region based approach. Also in literature their are models [1, 17] which utilized both edge as well as region information. Among traditional methods the famous and well known method is the Mumford-Shah (MS) energy functional [13], let $w_0 = w_0(x, y)$

be a given image then energy functional of MS model [13] is defined as:

$$\min_{w,r} E^{MS}(w,r) = \mathcal{H}^{n-1}(r) + \|w_0 - w\|_{L_2(\Omega)}^2 + \nu \int_{\Omega-r} |\nabla w|^2 dx dy, \quad (1.1)$$

where $w(x,y)$ is the smooth and segmented image closed to the given image $w_0(x,y)$, $\Omega \subset \mathbb{R}^n$ is a bounded set with the feature boundary and Lipschitz boundary set r , while \mathcal{H}^{n-1} is the $n-1$ dimensional Hausdorff measure, in case of two dimensional \mathcal{H}^1 represents the length of the segmented curve. MS model is computationally complex due to the use of \mathcal{H}^{n-1} term, therefore Chan-Vese (CV) [4] model adopted the piecewise constant segmentation model as follow:

$$E_{2D}^{CV}(r, u_1, u_2) = \mu \mathcal{H}^1(r) + \lambda_1 \|w_0 - u_1\|_{L_2(\Omega_{in})}^2 + \lambda_2 \|w_0 - u_2\|_{L_2(\Omega_{out})}^2, \quad (1.2)$$

where u_1 and u_2 are values of average intensities of w_0 inside and outside of r . λ_1 and λ_2 are constant parameters usually taken as one. Now in level set [15] formulation equation (1.2) can be expressed as:

$$E_{2D}^{CV}(\varphi, u_1, u_2) = \mu \mathcal{H}^1(\varphi) + \lambda_1 \|w_0 - u_1\|_{L_2(\Omega_{in})}^2 + \lambda_2 \|w_0 - u_2\|_{L_2(\Omega_{out})}^2, \quad (1.3)$$

where

$$\begin{aligned} \mathcal{H}^1(\varphi) &= \int_{\Omega} \delta(\varphi) |\nabla \varphi| dx dy, \\ \|w_0 - u_1\|_{L_2(\Omega_{in})}^2 &= \int_{\Omega} |w_0(x,y) - u_1|^2 H(\varphi) dx dy, \\ \|w_0 - u_2\|_{L_2(\Omega_{out})}^2 &= \int_{\Omega} |w_0(x,y) - u_2|^2 (1 - H(\varphi)) dx dy. \end{aligned} \quad (1.4)$$

As Heaviside function can not be differentiated at the origin therefore, a regularized Heaviside function is utilized [4];

$$H_{\epsilon}(y) = \frac{1}{2} \left(1 + \frac{2}{\pi} \arctan\left(\frac{y}{\epsilon}\right) \right), \quad \delta_{\epsilon}(y) = H'_{\epsilon}(y) = \frac{\epsilon}{\pi(\epsilon^2 + y^2)}.$$

CV model is actually designed for images having constant intensities and homogeneous regions therefore, it can not tackle images having variable intensities and regions. Several recent models can be seen which tried to overcome the limitation of the CV model [1, 5, 10, 18, 20] by utilizing image local information. But these models can tackle very less degree of inhomogeneity which is insufficient for accurate image segmentation [2, 16]. Therefore, in this paper a new model called Derived Image Data (DID) is presented for efficient segmentation of images suffering from high degree of inhomogeneity. In DID model we utilized local as well as global characteristics of a given image with a high pass filtering technique. Therefore, DID model can accurately segment images with clutter backgrounds, multi-intensity objects and intensity inhomogeneity.

Rest of the paper is arranged as follow; section 2 contains review of well known existing models. Section 3, contains our proposed DID model and an algorithm to solve it, while in section 4, a comparison among DID and others well known methods is done. Finally in section 5 some conclusive remarks are stated.

2. PREVIOUS WORKS

2.1. The Local Chan-Vese Model (LCV). As CV model is unable to detect objects having minute details therefore to overcome its limitations in such type of images Wang et al. proposed a new model known as local chan-veve (LCV) model [18]. In level set approach the energy functional of LCV model can be expressed as:

$$E_{2D}^{LCV}(\varphi, u_1, u_2, d_1, d_2) = \mu \mathcal{H}^1(\varphi) + \lambda_1 (\|w_0 - u_1\|_{L_2(\Omega_{in})}^2 + \|w_0 - u_2\|_{L_2(\Omega_{out})}^2) + \lambda_2 (\|w_0^* - d_1\|_{L_2(\Omega_{in})}^2 + \|w_0^* - d_2\|_{L_2(\Omega_{out})}^2), \quad (2.5)$$

where μ , λ_1 and λ_2 represents tuning parameters, $w_0^*(x, y)$ is smooth or difference image obtained through: $w_0^* = g_c * w_0(x, y) - w_0(x, y)$, with an averaging convolution operator g_c of window size $c \times c$. First term of equation (2.5) is regularization term which aim is to keep the curve smooth and tight around object boundaries. While the other two terms are data terms in which the term $\lambda_1 (\|w_0 - u_1\|_{L_2(\Omega_{in})}^2 + \|w_0 - u_2\|_{L_2(\Omega_{out})}^2)$ uses image global information, while the second term $\lambda_2 (\|w_0^* - d_1\|_{L_2(\Omega_{in})}^2 + \|w_0^* - d_2\|_{L_2(\Omega_{out})}^2)$ utilized image local information to capture minute details of the objects in an image. For the values of u_1, u_2, d_1, d_2 and φ equation (2.5) is minimized and the following equations are derived:

$$\begin{aligned} u_1(\varphi) &= \frac{\|w_0\|_{L_2(\Omega_{in})}^2}{\|\sqrt{w_0}\|_{L_2(\Omega_{in})}^2}, & u_2(\varphi) &= \frac{\|w_0\|_{L_2(\Omega_{out})}^2}{\|\sqrt{w_0}\|_{L_2(\Omega_{out})}^2}, \\ d_1(\varphi) &= \frac{\|w_0^*\|_{L_2(\Omega_{in})}^2}{\|\sqrt{w_0^*}\|_{L_2(\Omega_{in})}^2}, & d_2(\varphi) &= \frac{\|w_0^*\|_{L_2(\Omega_{out})}^2}{\|\sqrt{w_0^*}\|_{L_2(\Omega_{out})}^2}, \end{aligned} \quad (2.6)$$

and

$$\begin{aligned} \frac{\partial \varphi}{\partial t} &= \delta_\epsilon(\varphi) \left[\lambda_1 ((w_0 - u_2)^2 - (w_0 - u_1)^2) + \lambda_2 ((w_0^* - d_2)^2 - (w_0^* - d_1)^2) \right] \\ &\quad + \mu \delta_\epsilon(\varphi) \nabla \cdot \left(\frac{\nabla \varphi}{|\nabla \varphi|} \right) + \left(\nabla^2 \varphi - \nabla \cdot \frac{\nabla \varphi}{|\nabla \varphi|} \right), \end{aligned} \quad (2.7)$$

with initial and boundary conditions $\varphi(0, x, y) = \varphi_0(x, y)$, in Ω . LCV model perform better than CV model in images having low intensity of inhomogeneity but fails in those images having high degree of inhomogeneity. Since LCV model rely on difference image to capture local information [5, 10], but in case of high degree of variable intensities these information are insufficient for accurate segmentation of images.

2.2. Local Binary Fitting (LBF) Model. Another famous approach for the segmentation of inhomogeneous images was done by Li et al. by proposing a local binary fitting (LBF) model [10]. LBF model is a modified form of CV which introduced two smooth functions instead of constants in energy functional of CV model. These smooth functions has the localization property which try to fix image intensity near a given point x . In level set form, LBF model [10] is represented as:

$$E_{2D}^{LBF}(\varphi, g_1(x), g_2(x)) = \mu \mathcal{H}^1(\varphi) + \lambda_1 G_\sigma(x - y) \|w_0(y) - g_1(x)\|_{L_2(\Omega_{in})}^2 + \lambda_2 G_\sigma(x - y) \|w_0(y) - g_2(x)\|_{L_2(\Omega_{out})}^2, \quad (2.8)$$

λ_1 and λ_2 are setting parameters for assigning different weights, G_σ is a Gaussian kernel with localization property. While g_1 and g_2 are smooth functions to fix image intensity at a given pixel x . For the values of g_1 and g_2 equation (2. 8) is minimized and obtained as follow:

$$g_1 = \frac{G_\sigma * (H_\varepsilon(\varphi)w_0)}{G_\sigma * H_\varepsilon(\varphi)}, \quad (2. 9)$$

and

$$g_2 = \frac{G_\sigma * (1 - H_\varepsilon(\varphi))w_0}{G_\sigma * [1 - H_\varepsilon(\varphi)]}. \quad (2. 10)$$

By considering, g_1 and g_2 constant the minimization of energy functional (2. 8) with respect to φ gives as:

$$\begin{aligned} \frac{\partial \varphi}{\partial t} = & \delta_\varepsilon(\varphi) \left[(-\lambda_1(G_\sigma(y-x) \| w_0(y) - g_1(x) \|_\Omega^2) \right. \\ & \left. + \lambda_2(G_\sigma(y-x) \| w_0(y) - g_2(x) \|_\Omega^2)) + \nu \operatorname{div} \left(\frac{\nabla(\varphi)}{|\nabla(\varphi)|} \right) \right] \\ & + \mu(\nabla^2(\varphi) - \operatorname{div} \left(\frac{\nabla(\varphi)}{|\nabla(\varphi)|} \right)), \end{aligned} \quad (2. 11)$$

As LBF model mostly rely on image local characteristic therefore its results are better in images suffered from intensity inhomogeneity. But on the other hand it is very sensitive to its initial contour and the choice of standard deviation σ , thus even small changes in these terms leads to unsuccessful and undesire segmentation results. Therefore, such issues limit the use of LBF model [19].

2.3. Region-based model via Local Similarity Factor(RLSF). A recent approach to segment intensity inhomogeneous images suffered from noise has taken by Niu et al. [14] by introducing a local similarity factor in a region base active contour model. Local similarity factor actually relies on the local spatial distance within a local window and local intensity difference to guide the motion of active contour [2, 12]. The overall energy functional of RLSF model in level set formulation can be expressed as:

$$\begin{aligned} E_{2D}^{RLSF}(\varphi, lu_1(x), lu_2(x)) = & \mu \mathcal{H}^1(\varphi) + \lambda_1 \left\| \frac{w_0(y) - lu_1(x)}{d(y, x)} \right\|_{L_2(\Omega_{in})}^2 \\ & + \lambda_2 \left\| \frac{w_0(y) - lu_2(x)}{d(y, x)} \right\|_{L_2(\Omega_{out})}^2, \end{aligned} \quad (2. 12)$$

where d is the spatial Euclidean distance between two pixels. $lu_1(x)$ and $lu_2(x)$ are the local average intensity values inside and outside of the active contour, defined as within local regions as:

$$lu_1(x) = \left\| \frac{M(x, y)w_0(y)}{M(x, y)} \right\|_{L_2(\Omega_{in})}^2, \quad lu_2(x) = \left\| \frac{M(x, y)w_0(y)}{M(x, y)} \right\|_{L_2(\Omega_{out})}^2 \quad (2. 13)$$

Here, $M(x, y)$ is known as mask which aim is to define local regions in order to use the background and foreground information in terms of smaller local regions [14] and is define mathematically as:

$$M(x, y) = \begin{cases} 1 & d(y, x) < r, \\ 0 & \text{otherwise.} \end{cases} \quad (2. 14)$$

where d is the spatial Euclidean distance between the pixel y and the center x of a local region and r is a parameter defining the maximum size of the local region. By using the gradient descent flow method, minimization of the energy functional (2.12) with respect to φ leads to corresponding variational level set formulation, for more details interested readers are referred to [14]. As RLSF method completely avoids the pre-processing steps typical of region-based contour model segmentation, resulting in a higher preservation of image details. But this algorithm completely relies on its mask and even a slight change or carelessness in taking mask leads to unfavourable segmentation results as discuss later.

3. PROPOSED METHOD

In this section we present our proposed method by utilizing multi images data to guide the motion of active contour. For this purpose we utilized three images i.e. original image, smooth image and difference image. To obtain smooth image we design the following functional:

$$(\beta g_1 + (1 - \beta)u_1)H(\phi) + (\beta g_2 + (1 - \beta)u_2)(1 - H(\phi)). \quad (3.15)$$

Here g_1 and g_2 represent spatially varying fitting functions as obtained in equations (2.9) and (2.10) where u_1 and u_2 are the average intensities as used in CV model [4]. $\beta \in [0, 1]$ is the scaling parameter which keep balance between the spatially varying fitting functions and the averages. On the other hand to calculate the difference image we utilized the following functional:

$$w_0^* = g_c * w_0 - w_0 \quad (3.16)$$

where g_c is a convolution operator of window size $c \times c$. Figure 1 demonstrates how these two functional (3.15) and (3.16) works on different types of images having intensity inhomogeneity, noise and multi-background. In figure 1 first column represent observed images, second column represent the fitting smooth image obtained through (3.15) while last column represents the difference image obtained from (3.16). Figure 1(a) is the observed image which is suffered from intensity inhomogeneity, figure 1(d) is the given noisy image and figure 1(g) is a clutter multi background image. While figures 1(b), 1(e) and 1(h) are the filter images obtained through (3.16). In contrast figures 1(c), 1(f) and 1(i) are the difference images obtained through (3.16). Now it is very clear that the smooth and difference images are more prominent as compared to the given images and is more convenient for image segmentation.

Therefore, based on these observations we designed the following energy functional:

$$\begin{aligned} E_{2D}^{DID}(\varphi, d_1, d_2, U_1, U_2) &= \mu(\text{length term}) + \nu(\text{regularity term}) \quad (3.17) \\ &+ \lambda_1(\|w_0 - U_1\|_{L_2(\Omega_{in})}^2 + \|w_0 - U_2\|_{L_2(\Omega_{out})}^2) \\ &+ \lambda_2(\|w_0^* - d_1\|_{L_2(\Omega_{in})}^2 + \|w_0^* - d_2\|_{L_2(\Omega_{out})}^2), \end{aligned}$$

where U_1 and U_2 are define as: $U_1(u_1, g_1) = (\beta g_1 + (1 - \beta)u_1)$ and $U_2(u_2, g_2) = (\beta g_2 + (1 - \beta)u_2)$; where $0 \leq \beta \leq 1$. The data term $\|w_0 - U_1\|_{L_2(\Omega_{in})}^2 + \|w_0 - U_2\|_{L_2(\Omega_{out})}^2$ is utilizing image data indirectly in the form as illustrated in the second column of figure 1. This data term robust DID to clearly identify image boundaries from background. In contrast, the data term $\|w_0^* - d_1\|_{L_2(\Omega_{in})}^2 + \|w_0^* - d_2\|_{L_2(\Omega_{out})}^2$ helps DID to tackle intensity inhomogeneity and classify accurately object boundaries from background. This

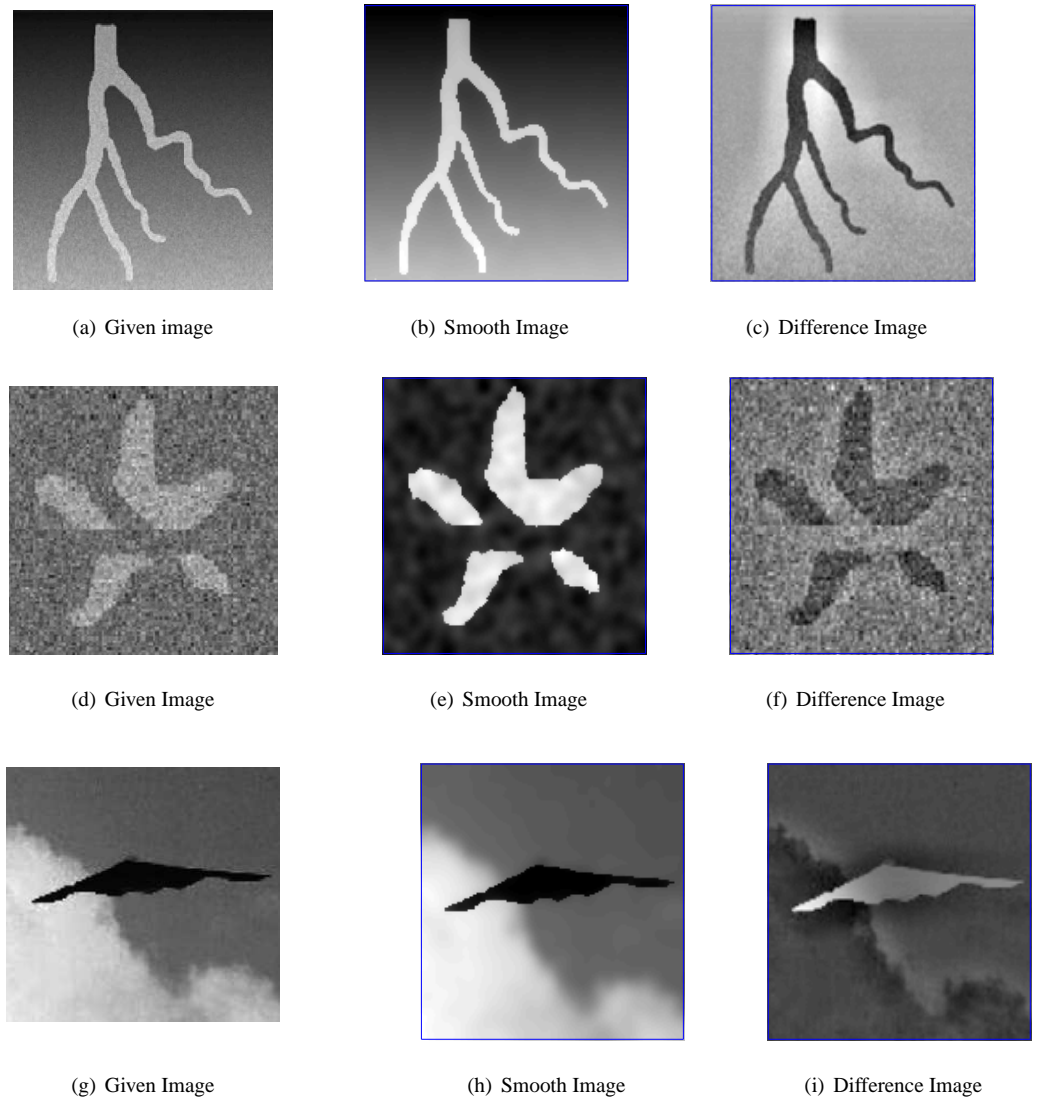


FIGURE 1. Illustration of different images and their corresponding smooth and difference images. Smooth images are obtained from equation (3.15), while difference images are obtained through equation (3.16).

data term uses image data in the form as presented in the last column of figure 1. Thus the

overall energy functional of DID model can be expressed in the form:

$$\begin{aligned} E_{2D}^{DID}(\varphi, d_1, d_2, U_1, U_2) &= \mu \int_{\Omega} \delta(\varphi) |\nabla \varphi| dx dy + \nu \int_{\Omega} \frac{1}{2} (|\nabla \varphi| - 1)^2 dx dy \\ &+ \lambda_1 (\|w_0 - U_1\|_{L_2(\Omega_{in})}^2 + \|w_0 - U_2\|_{L_2(\Omega_{out})}^2) \\ &+ \lambda_2 (\|w_0^* - d_1\|_{L_2(\Omega_{in})}^2 + \|w_0^* - d_2\|_{L_2(\Omega_{out})}^2), \end{aligned} \quad (3.18)$$

Now to find Euler Lagrange equation for the functional (3.18) keep u_1, u_2, d_1, d_2, g_1 and g_2 constant and minimizing equation (3.18) with respect to φ then we have:

$$\begin{aligned} &\left[\mu \delta_{\epsilon}(\varphi) \operatorname{div} \left(\frac{\nabla(\varphi)}{|\nabla(\varphi)|} \right) + (\nabla^2(\varphi) - \operatorname{div} \left(\frac{\nabla(\varphi)}{|\nabla(\varphi)|} \right)) \right. \\ &\left. + \delta_{\epsilon}(\varphi) \left(\lambda_1 ((w_0 - U_1)^2 - (w_0 - U_2)^2) + \lambda_2 ((w_0^* - d_1)^2 - (w_0^* - d_2)^2) \right) \right] = 0. \end{aligned} \quad (3.19)$$

Further by considering the partial differential equation (3.19) as a steady state solution of the evolution equation as written below:

$$\begin{aligned} \frac{\partial \varphi}{\partial t} &= \left[\left(\mu \delta_{\epsilon}(\varphi) \operatorname{div} \left(\frac{\nabla(\varphi)}{|\nabla(\varphi)|} \right) + (\nabla^2(\varphi) - \operatorname{div} \left(\frac{\nabla(\varphi)}{|\nabla(\varphi)|} \right)) \right) \right. \\ &\left. + \delta_{\epsilon}(\varphi) \left(-\lambda_1 (w_0 - U_1)^2 + \lambda_1 (w_0 - U_2)^2 - \lambda_2 (w_0^* - d_1)^2 + \lambda_2 (w_0^* - d_2)^2 \right) \right], \end{aligned} \quad (3.20)$$

With the initial and boundary condition define as $\varphi_0(0, x, y) = \varphi(x, y)$, in Ω , and $\frac{\partial \varphi}{\partial \vec{n}} = 0$, on $\partial\Omega$, respectively. Where the exterior normal vector to the boundary $\partial\Omega$ is represented by \vec{n} .

Algorithm to solve (3.20)

The principal steps for the algorithm to solve DID model are listed as follows:

- 1st Step. Input the observed image w_0 .
- 2nd Step. Take an initial guess in the form of a contour.
- 3rd Step. Solve (2.6), (2.9), (2.10) to update c_i, d_i, g_i for $i=1, 2$.
- 4th Step. Initiate the function φ as given in equation (3.20) with the numerical scheme as given in [8, 11].
- 5th Step. Check convergence of function φ : if converged, stop; else return to 2nd Step.
- 6th Step. Find out the segmented portion from $\varphi < 0$.

4. EXPERIMENTAL RESULTS

This section is devoted to the experimental study of DID model and its comparison with the LBF and LCV models. All the experiments presented in this section were taken out on MATLAB version 7.9.0 using core i3 personal computer with 2GB RAM, 2.40 GHz processor, and windows 8 operating system. First of all we checked the performance of DID on various type of images including synthetic, real world challenging, variable intensities images, and images having multi intensity objects. Then we compared the performance of DID with RLSF (for this method the sizes of all images are taken as $[111 \times 110]$ for achieving better segmentation results), LCV and LBF models on different types of images including real world, noisy as well as synthetic images to ensure that our model perform better than these models. Further for qualitative analysis, we used Jacard similarities to

compare the performance of DID with other well known models. Finally, we have done experiments on color images to ensure that the proposed model also perform very well on color images which is our future project as well. For each experiment the value of λ_1 is taken as 1 while λ_2 and β are tune according to each image for our proposed model.

Figure 2 contain six different types of images suffered from intensity inhomogeneity and having multi-intensity objects in background, in which the first and third rows represent the observed images with initial contour while the second and forth row shows its segmented results. As figures 2(a), 2(b) and 2(c) are synthetic, blood vessel and real aircraft images respectively, suffered from intensity inhomogeneity. While figures 2(g), 2(h) and 2(i) are multi-phase images in which 2(h) is similar to 2(g) but intensity inhomogeneity is added to image domain which make it more complicated. Now it can be clearly observed from figures 2(d), 2(e), 2(f), 2(j), 2(k) and 2(l) that DID model successfully segmented the given images without any lose of minute details and capture the accurate boundaries of the objects in the given images. Parameters used for these experiments are $\lambda_2 = 0.01$ and $\beta = 0.7$ for all images except 2(a) and 2(i) for which the values of λ_2 and β are taken as 1.

In figure 3 a comparison between RLSF and proposed technique is presented on noisy images, in which first row present given images with initial contour, second row shows results of RLSF while last row are the results of DID model. The unsuccessful and undesirable results of RLSF method can easily be observed from figures 3(d), 3(e) and 3(f) while figures 3(g), 3(h) and 3(i) prove successful segmentation results of DID model. Parameters used for proposed technique are $\beta = 0.7$, $\lambda_2 = 0.1$ for figure 3(g) while for figures 3(h) and 3(i) $\beta = 0.1$ and $\lambda_2 = 0.01$. In figure 4 a comparison among LCV, RLSF and DID model is shown on four different images in which the first two i.e. 4(a) and 4(e) are real world plane images and having clouds in the background which make the background cutter and complex. While the last two images i.e. 4(i) and 4(m) are multi-phase images having average intensity background and multi-intensity objects in the foreground. In figure 4 first column represents original images with initial guess, second, third and forth columns display results of LCV, RLSF and DID models, respectively. Figure 4(b) clearly shows that LCV model divided the image into two portions instead of capturing object in the foreground while figure 4(c) exhibits the unsuccessful results of RLSF model, in contrast the accurate result of DID is clear from figure 4(d). Again from figure 4(f) it can be easily observed that LCV model capture an extra region in the background along with the object, similarly, RLSF model also fails in segmentation and capture only small portion as shown in figure 4(g). On the other hand DID model extract object with minute details in it as displays in figure 4(h). Similarly, LCV and RLSF models fail to segment multi-phase images as shown in figures 4(j), 4(n) and 4(k), 4(o) respectively. While in comparison the successful results of DID model in all these mentioned images can be verified from figures 4(l) and 4(p). Parameters used for figures 4(d), 4(l) and 4(p) are $\beta = 1$ and $\lambda_2 = 0.0001$ while for figure 4(h) $\beta = 0.8$ and $\lambda_2 = 1$.

Figure 5 demonstrates comparison among LCV, LBF and DID model on two images in which 5(a) is a jet fighter image having complex background while 5(e) is a synthetic fish image having severe intensity inhomogeneity. The unsuccessful result of LCV and LBF models can be clearly seen from 5(b) and 5(c) respectively, on jet fighter image, on the other hand accurate result of DID can be easily verified from 5(d). Figure 5(e) is a synthetic image of fish which is suffered from sever intensity inhomogeneity in which both

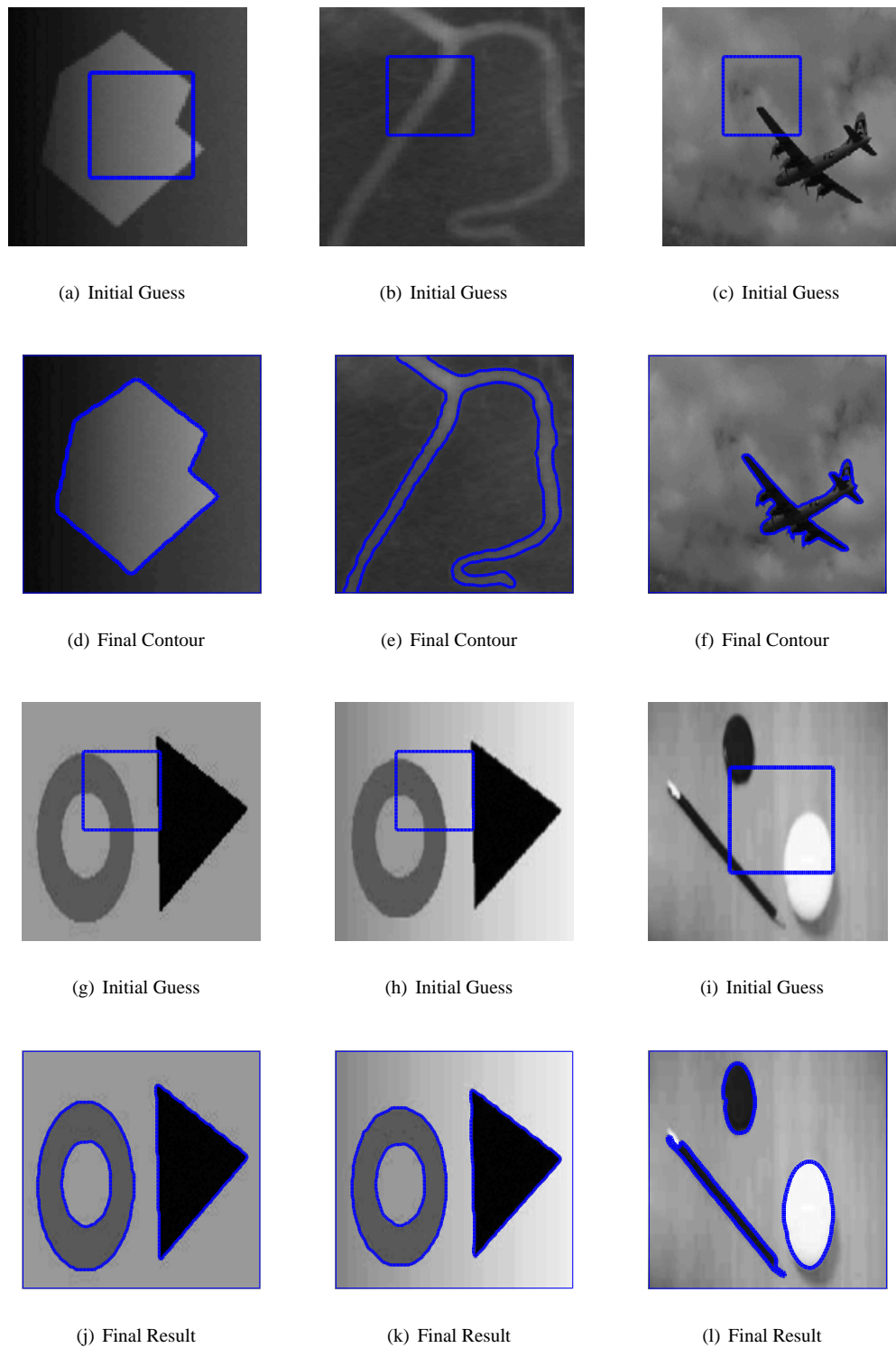


FIGURE 2. This figure demonstrate the performance of DID on synthetic, real and multi-intensity objects images where first and third rows show given images with initial contour while second and last row presents segmentation results.

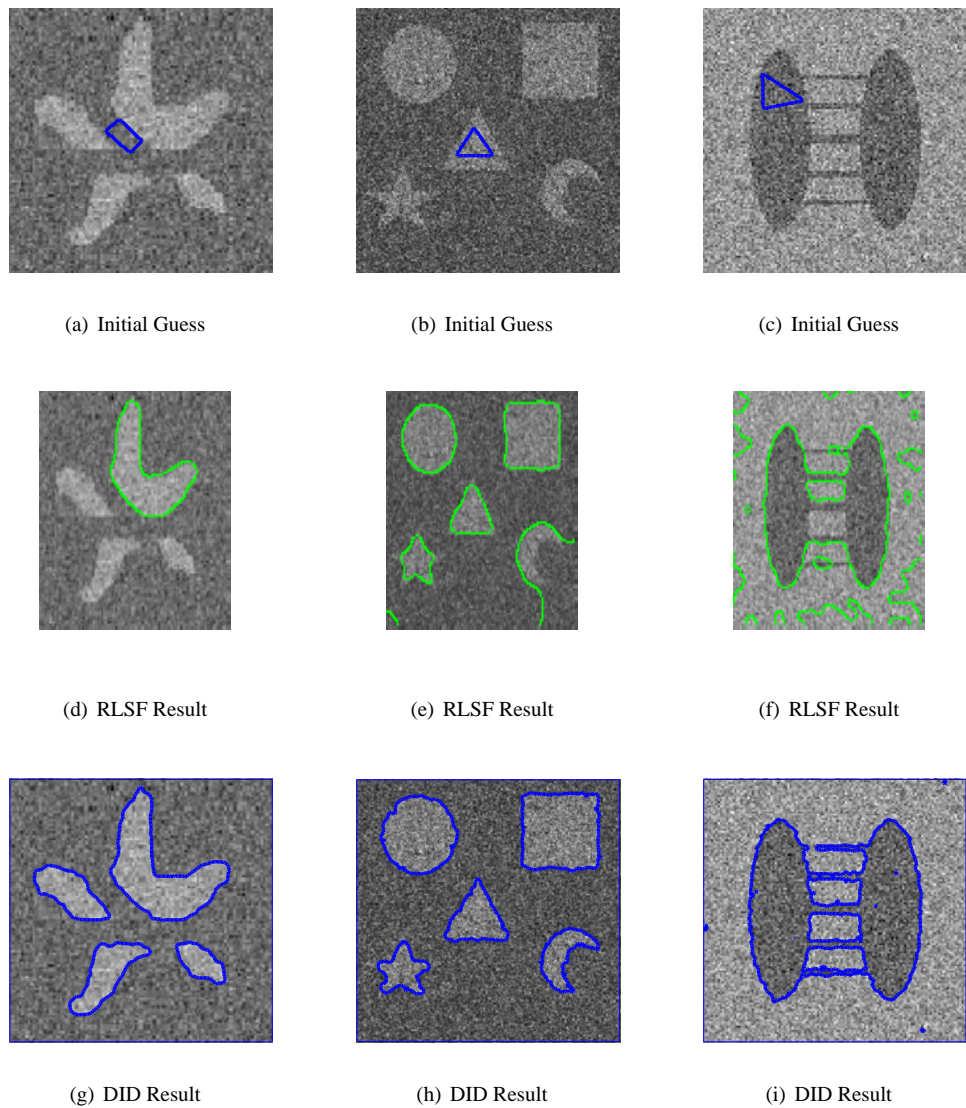


FIGURE 3. This figure demonstrate segmentation results of DID model on multi-phase inhomogeneous and noisy images. First and third row shows initial contour, while the corresponding segmented results are shown in second and last row, respectively.



FIGURE 4. Comparison of LCV, RLDF and DID models on various images having clutter background images and multi-pase images. First column presents initial guess, second, third and forth columns show results of LCV, RLDF and DID models, respectively.

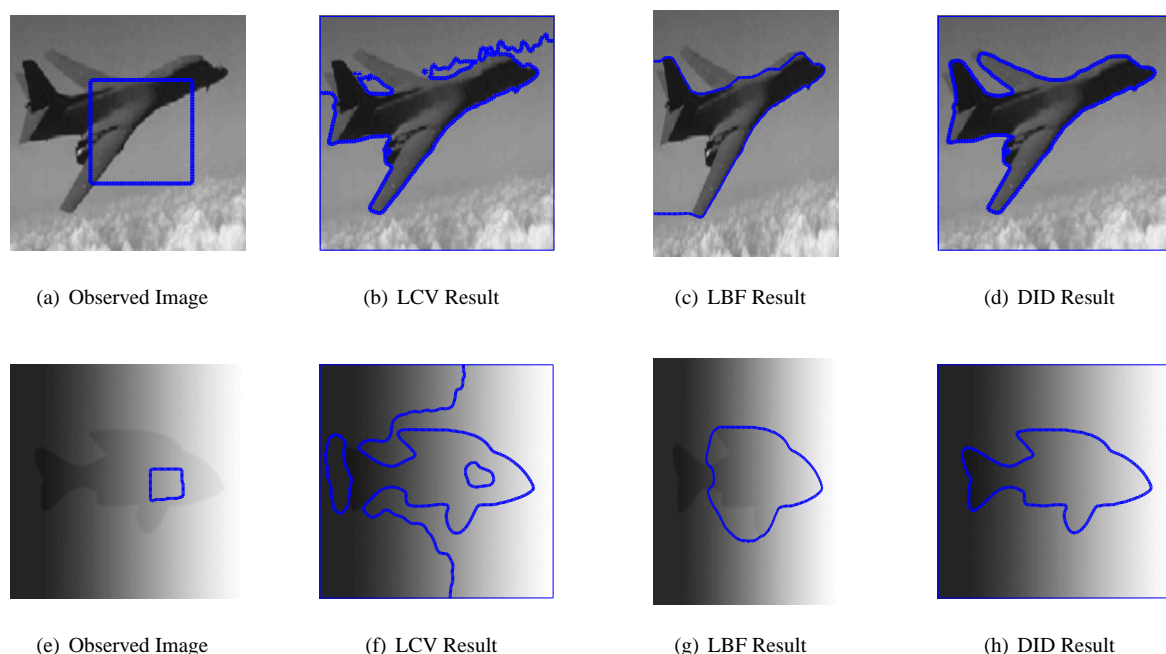


FIGURE 5. This figure demonstrates comparative performance of LCV, LBF and DID models on low and high degree of intensity inhomogeneous images.

the models LCV and LBF are fail to segment it as shown in 5(f) and 5(g). In contrast, the successful and accurate segmentation result of DID can be seen in 5(h). Parameters used for jet fighter are $\beta = 0.7$ and $\lambda_2 = 0.0005$ while for synthetic fish image $\beta = 1$ and $\lambda_2 = 0.0001$.

4.1. Qualitative Analysis. For qualitative analysis of DID we used Jaccard Similarity (JS) on a set of two images as shown in figure 6. Consider we have an observed image w_0 with ground truth G and segmented result S . Then the intersection ratio of two regions S and G is termed as JS. Value of JS varies from 0 to 1 and if the value is close to 1 then the segmented result is more accurate and vise versa. Figure 6 consists on two images i.e. plane 1 and plane 2 in which 6(a) and 6(c) are given images while 6(b) and 6(d) are their ground truth (GT) images respectively, which are obtained manually. In addition, the segmentation results for plane 1 and plane 2 images of LCV, LBF, RLSF and DID models are also displayed in figure 6. On the other hand JS graph for these test images are shown in figure 7 in which first, second, third and forth columns shows JS graph for LCV, LBF, RLSF and DID models, respectively. It can be easily observed from figure 7 that DID model achieve better segmentation results with less number of iterations than other methods. In all the JS graph of figure 7, horizontal line shows the number of iterations while the vertical

line shows the correspond JS value. Furthermore, in table 1 we demonstrate separately the JS value for each image and the corresponding model used for it. Now from table 1 it can be easily observed that the performance of DID model is better than the others one.

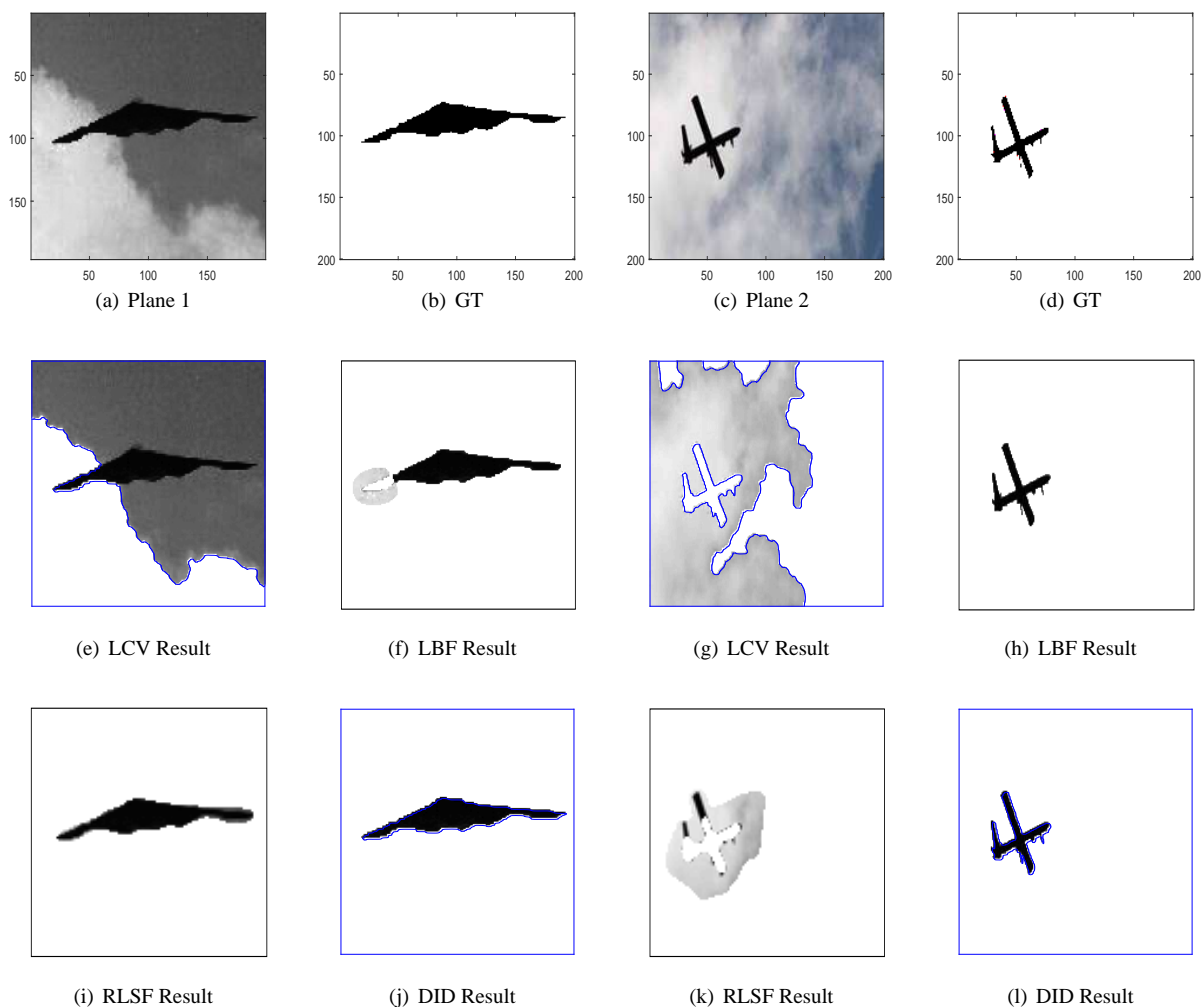


FIGURE 6. Segmentation results of LCV, LBF, RLSF and DID models on two images, i.e., plane 1 and plane 2 with their ground truth (GT) images.

4.2. Performance on Color Images. Finally, to ensure the performance of DID model on real world vector valued images we have done four experiments on color images as

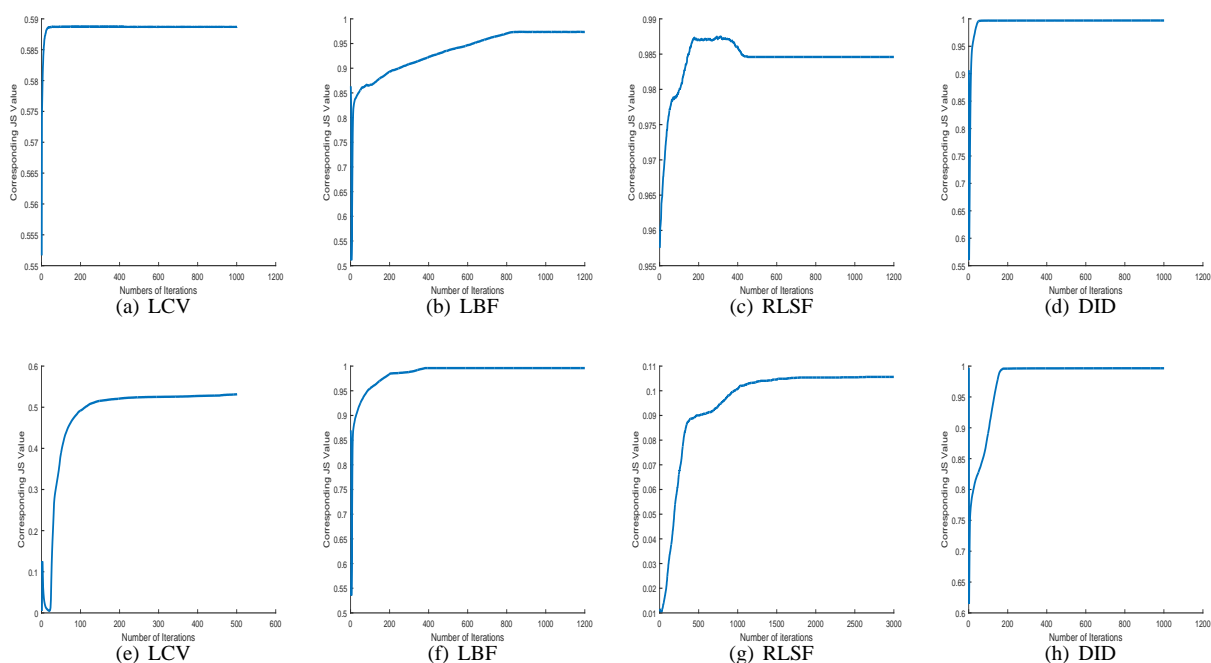


FIGURE 7. Comparison of four methods using Jaccard Similarity. First row represents the JS graph of Plane 1, while second row represents JS graph of plane 2 image.

Observed Image	JS of LCV	JS of LBF	JS of RLSF	JS of DID
Plane 1 Image	0.5887	0.9954	0.9846	0.9954
Plane 2 Image	0.5549	0.9959	0.1056	0.9965

TABLE 1. This table demonstrate the qualitative analysis of LCV, LBF, RLSF and DID models using Jaccard similarity on two different images as given in figure 6.

shown in figure 8. In figure 8 first column represent given color images with initial contour while second and third columns show final contour and its corresponding segmented results, respectively. Figures 8(a) and 8(d) are the car number plates images having light in the background which creates difficulty in segmentation process. But from figures 8(c) and 8(f) it is clear that DID model perform well in segmenting such type of images and is able to extract minute details present in it. Figure 8(g) is a vector valued hardware image having unilluminated object in the background but DID model also segment it very well and extracted object from the observed image as shown in figure 8(i). On the other hand

8(j) is thermal image of four men, having bright background now it can be observed from 8(l) that DID model extract the objects from the given image with all of its features.

5. CONCLUSION

A new model is designed for the accurate segmentation of variable intensity images which is based on image filtering techniques and by relying on image local as well as global information. The novel model is able to handle different types of real world and synthetic images by employing the new set of technique. Experimental section also witnessed that our DID model perform better than those of LCV, LBF and RLSF models. Moreover, the proposed DID model is also tested on various color images to show that DID model also preserve its performance on vector valued images as well.

6. ACKNOWLEDGMENTS

We greatly acknowledge all reviewers for their constructive criticism, invaluable comments that greatly enhance this article. I am also thankful to Mr. Zia Ul Mabood, for proofreading.

7. CONFLICT OF INTEREST

All the authors in this paper contributed equally and have no conflict of interest to disclose.

REFERENCES

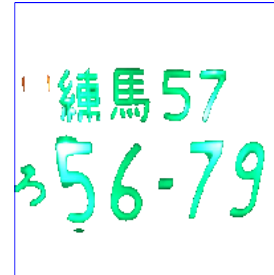
- [1] H. Ali, N. Badshah, K. Chen, G.A. Khan, *A Variational Model with Hybrid Images Data Fitting Energies for Segmentation of Images with Intensity Inhomogeneity*, Pattern Recognition **51**, (2016) 27–42.
- [2] N. Badshah, K. Chen, *Image Selective Segmentation Under Geometrical Constraints Using an Active Contour Approach*, Communication and Computational Physics **07** No. 4, (2010) 759–778.
- [3] V. Caselles, R. Kimmel and G. Sapiro, *Geodesic active contours*, International Journal of Computer Vision **22**, No. 1 (1997) 61–79.
- [4] T. F. Chan and L. A. Vese, *Active contours without edges*, IEEE Transactions on Image Processing **10**, No. 2 (2001) 266–277.
- [5] S. Z. Fishan, L. Mabood, H. Ali and N. Badshah, *Active Contour Model Based on Local Signed Pressure Force Functions*, Punjab University Journal of Mathematics **51**, No. 4 (2019) 113–129.
- [6] C. Gout, C. L. Guyader and L. A. Vese, *Segmentation under geometrical conditions with geodesic active contour and interpolation using level set method*, Numerical Algorithms **39**, (2005) 155–173.
- [7] C. L. Guyader and C. Gout, *Geodesic active contour under geometrical conditions theory and 3D applications*, Numerical Algorithms **48**, (2008) 105–133.
- [8] M. Jeon, M. Alexander, W. Pedrycz and N. Pizzi, *Unsupervised hierarchical image segmentation with level set and additive operator splitting*, Physical Review Letters **26**, No. 10 (2005) 1461–1469.
- [9] M. Kass, A. Witkin and D. Terzopoulos, *Active contours models*, International Journal of Computer Vision (1988) 321–331.
- [10] C. M. Li, C. Kao, J. Gore and Z. Ding, *Implicit active contours driven by local binary fitting energy*, IEEE Conference on Computer Vision and Pattern Recognition, 2007.
- [11] T. Lu, P. Neittaanmaki and X. C. Tai, *A Parallel Splitting up Method and its Application to Navier-Stokes Equations*, Appl. Math. Lett, **4** No. 2, (1991) 25–29.
- [12] L. Mabood, H. Ali, N. Badshah, K. Chen and G. A. Khan, *Active contours textural and inhomogeneous object extraction*, Pattern Recognition **55**, (2016) 87-99.
- [13] D. Mumford and J. Shah, *Optimal approximation by piecewise smooth functions and associated variational problems*, Communications on Pure Applied Mathematics **42**, (1989) 577–685.



(a) Observed Image



(b) Final Contour



(c) Extracted Foreground



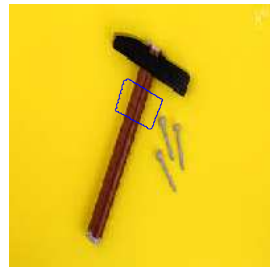
(d) Observed Image



(e) Final Contour



(f) Extracted Foreground



(g) Observed Image



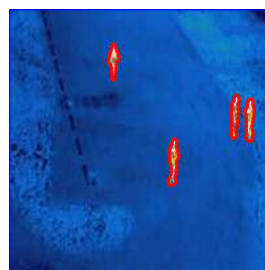
(h) Final Contour



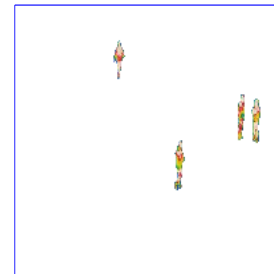
(i) Extracted Foreground



(j) Observed Image



(k) Final Contour



(l) Extracted Foreground

FIGURE 8. Performance of DID model on vector valued images where first column display observed images while second and last columns shows the segmented and foreground extracted images, respectively.

- [14] S. Niu, Q. Chen, L. D. Sisternes, Z. Ji, Z. Zhou and D. L. Rubin, *Robust Noise Region-based Active Contour Model via Local Similarity Factor for Image Segmentation*, Pattern Recognition **61**, (2017) 104-119.
- [15] S. Osher and J. A. Sethian, *Fronts propagating with curvature-dependent speed: algorithms based on Hamilton-Jacobi formulations*, J. Comput. Phys. **79**, No. 1 (1988) 12-49.
- [16] L. A. Vese and T. F. Chan, *A multiphase level set framework for image segmentation using the Mumford and Shah model*, Int. J. Computer Vision **50**, No. 3 (2002) 271-293.
- [17] W. Wang, Y. Wang, Y. Wu, T. Lin, S. Li and B. Chen, *Quantification of Full Left Ventricular Metrics via Deep Regression Learning With Contour-Guidance*, IEEE Access **7**, (2019) 47918-47928.
- [18] X. F. Wang, D. S. Huang and H. Xu, *An efficient local Chan-Vese model for image segmentation*, Pattern Recognition **43**, (2010) 603-618.
- [19] Y. Wu and C. He, *A Convex Variational Level Set Model for Image Segmentation*, Signal Processing **106**, (2015) 123-133.
- [20] Z. Zhang, C. Duan, T. Len and S. Zhou, *GVFOM: A Novel External Force for Active Contour Based Image Segmentation*, Information Sciences **4506**, (2020) 1-18.
- [21] S. Zhou, Y. Lu, N. Li and Y. Wang, *Extension of the Virtual Electric Field Model Using Bilateral-like Filter for Active Contours*, Signal, Image and Video Processing **13**, No. 6 (2019) 1131-1139.